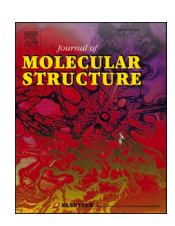
ELSEVIER

Contents lists available at ScienceDirect

Journal of Molecular Structure

journal homepage: www.elsevier.com/locate/molstr





Novel series of hydrazones carrying pyrazole and triazole moiety: Synthesis, structural elucidation, quantum computational studies and antiviral activity against SARS-Cov-2

D.V. Geetha ^a, C.L. Sharath ^b, N. Shivakumar ^c, B.N. Lakshminarayana ^{c,*}, K.M. Chandini ^d, K. Balakrishna ^{b,e}

- ^a Department of Physics, Mysore University School of Engineering, Manasagangotri, University of Mysore, Mysuru 570006, Karnataka, India
- ^b Department of Studies in Chemistry, Mangalore University, Mangalagangothri, Managaluru 574199, Karnataka, India
- Department of Studies in Chemistry, Mangaiore University, Mangalagangouri, Managaluru 574199, Karnataka, India ^c Department of Physics, Adichuchanagiri Institute of Technology, Chikkamagaluru, 577102, Karnataka, India
- d Department of Studies in Physics, Manasagangotri, University of Mysore, Mysuru 570006, Karnataka, India
- ^e Department of Chemistry, Yenepoya (Deemed to be)University, YIASCM Campus, Mangalore, Karnataka, India

ARTICLE INFO

Keywords: DFT RDG QTAIM Molecular docking

ABSTRACT

The novel series of hydrazones carrying both pyrazole and triazole moiety were synthesized and characterized using single crystal X-ray diffraction studies. It is found that the compound crystallizes in the triclinic system in the space group $P1^-$. Hirshfeld analysis was carried out to visualize the noncovalent intermolecular interactions which are responsible for molecular packing in the crystal. Further, density functional theory (DFT) calculations were used to calculate optimized molecular structure, stability, and a few of the quantum chemical parameters. Derived results are in good agreement with the experimentally obtained results. Analysis of frontier molecular orbitals (HOMO and LUMO) and their energy gap of the optimized structure revealed that the compound is stable in the gaseous state. Molecular electron densities, and electrostatic potential maps provide the reactive site and charge distribution of triazole group. Quantum theory of atoms in molecules (QTAIM) and reduced density gradient (RDG) analysis were carried out to explore the weak interactions present in the molecule. In addition, the synthesized compound was investigated as an inhibitor for $SARS\ CoV-2$ protease using in-silico molecular docking analysis to understand the mode of binding. The docking results showed the good binding score with Mpro protease 6LU7. Further, molecular dynamics (MD) were carried out for the best hit docked complexes.

1. Introduction

Pyrazoles belong to the class of heterocyclic compounds characterized by the presence of two nitrogen atoms adjacent to three carbon atoms in a five-membered aromatic ring structure. Due to their wide spectrum of biological activities, pyrazole has become the most important unit of drug discovery and in the pharmaceutical industry [1]. The vast applications of pyrazoles and triazoles make them one of the important heterocyclic compounds.

Pyrazoles and 1,2,4 -triazoles serve as crucial scaffolds in building important molecules having varied biological activities such as anti-bacterial [2], antifungal [3], anti-inflammatory [4], anthelmintic [5], anti-inflammatory [6], tumorigenesis [7], antioxidant [8], antidepressant [9], antiviral [10], antidiabetic [11], analgesic [12], anticancer

[13], antitubercular [14]. Further, pyrazole derivatives act as oestrogen receptor binding [15], neuroprotective [16], antineoplastic agents [17].

Literature survey reveals that hydrazones and their derivatives are the potential candidates for antiviral activities in the drug discovery [18]. To investigate the biological activities against *SARS corona* virus we focussed on the synthesis of these compounds.

December 2019 was the era of the first outbreak of corona virus infection, which was reported in Wuhan, China. The infection was huge enough to spread worldwide in a short duration, which caused the death of enormous people. Then the trail has begun for searching potent antivirus, which could control the infection. The infectious virus was named as *SARS-CoV-2* because its RNA genome shares 82 percent of its sequence with the *SARS Corona virus* [19]. The infection was first found in Wuhan's Huanan seafood and cattle market, later on the virus gets

^{*} Corresponding author at: Department of Physics, Adichuchanagiri Institute of Technology, Chikkamagaluru 577102, Karnataka, India. *E-mail address:* lakshminarayanabn@aitckm.in (B.N. Lakshminarayana).

Scheme 1. 4-(((5-(2,4-dichlorophenoxy)-3-methyl-1-phenyl-1H-pyrazol-4-yl)methylene)amino)-5-propyl-4H-1,2,4-triazole-3-thione (7c).

succeeded in entering into the human bod. The transmission of virus from human-human was so meteoric which leads to rise the number of patients to dramatically.

The disease caused by the corona virus commonly known as "COVID-19" became the global disaster leads to acute respiratory illness. The pandemic has affected the lives and the work of many people around the world. As of April 9th, there were more than 1.5 million diseased individuals with a 5.9 % mortality rate. By April 2021, the number has been increased dramatically, over140 million infections were reported with 3 million fatalities globally [20].

Later on, several variants of *SARS-CoV-2* virus have been emerged. This caused the significant public health threat for the society, the need of antiviral medications which could fight against the viruses were required to enhance the immunity and to protect high-risk groups [21]. Similar to other corona viruses, *SARS-CoV-2* also impacts the human the respiratory system and causes severe pneumonia, which requires ventilatory assistance and intensive care, especially in the elderly and immunocompromised patients [22].

SARS-CoV-2 belongs to the beta group of corona viruses, which is an RNA virus with only one strand. It contains structural proteins, such as spike-like protein S and lipid membranes, as well as M protein (membrane), N protein (nucleocapsid), and envelope (E) protein that gives an envelope appearance. The S spike protein binds to the angiotensin-converting enzyme 2 (ACE2) receptor on mammalian lung cells, allowing the virus's RNA genetic material to be released into the host cells [23]. Four non-structural proteins are found in the virus: papain-like (PLpro) and CoV main proteases [Mpro], RNA polymerase, and helicase [24]. The virus's transcription and replication are aided by both proteases (PLpro and Mpro). Protease Mpro, spike protein and RNA-dependent RNA polymerase (RdRp) are identified as the most promising targets [25].

The replicase genes encode two polyproteins important for effective viral replication and transcription [26]. The Mpro enzyme has become the main target to develop antiviral drugs against *SARS-CoV-2* as no host protease recognizes the Mpro recognition sequence. Protease inhibitors efficiently hinder the coronavirus multiplication and proliferation by obstructing the post-translational processing of essential viral polypeptides [27].

By considering the fact that anticorona virus therapeutics may hinder the Mpro's catalytic activity and due to the wide spread of *SARS-CoV-2*, it was crucial to look for novel potential therapeutic agents which serve as efficient antivirals in controlling the pandemic. To discover new

antiviral drugs, molecular docking, and drug-likeness evaluations of potential compounds were necessary. *In silico* studies were helpful in identifying the potent drug candidates which bind closely to the Mpro of the *SARS-CoV-2* catalytic site and limit its proteolytic activity [28].

Literature revealed that the Inhibition of COVID-19 Mpro by triazole and pyrazole derivatives offers a promising strategy in the development of effective treatments against COVID-19. When the COVID-19 Mpro protein is inhibited by these compounds, it subdues the replication of the virus and the body develops immunity against the virus [29]. Most of the triazole derivatives exhibited potent cellular anti-COVID-19 activity which led to reduced viral multiplication by more than 50 % with no or weak cytotoxic effect on harbouring cells. [30,31]. Hydrazone compounds having pyrazole and triazole moiety show good binding affinities to SARS-CoV-2 Mpro [32,33].

The macromolecular structures of coronavirus and its known variants are already available. We need to seek for *anti-SARS-CoV-2* drugs, which could hinder or halt virus replication. In this study, we have investigated the binding affinities of hydrazoneshaving pyrazole and triazole scaffolds against the *SARS-CoV-2* main protease (M^{pro}) later these may be used as a potential drug candidates for the same.

Prompted by these findings, herein we have described the synthesis, X-ray crystallography studies, DFT calculations, Hirshfeld surface analysis, MEP analysis, QTAIM calculations of novel series of hydrazones carrying both pyrazole and triazole moiety. In addition, we have reported *in-silico* molecular docking studies and molecular dynamics against *SARS-CoV-2* main protease.

2. Experimental procedure

Synthesis of 5-methyl-2-phenyl-2,4-dihydro-3H-pyrazol-3-one (3)

Phenyl hydrazine (1) (5.4 g, 0.05 mol) and redistilled ethyl acetoacetate (2) (6.5 g, 0.05 mol) were taken in a china dish, and the reaction mixture was heated on a water bath with continuous stirring for 3 h. The reaction was brought to room temperature, the contents were filtered washed with diethyl ether to remove the coloured impurities. The solid obtained was dried and recrystallized from hot water. m.p: $127 \,^{\circ}$ C [34]. $127 \,^{\circ}$ C), yield 78 %.

Synthesis of 5-chloro-3-methyl-1-phenyl-1H-pyrazole-4-carbaldehyde (4)

N,N-dimethyl formamide (7.3 g, 0.1 mol) was taken in a 250 ml round bottom flask fitted with a dropping funnel and cooled to 0–5 $^{\circ}$ C.

To this phosphorous oxychloride (15 g, 0.1 mol) was added dropwise through dropping funnel. 5-Methyl-2-phenyl-2,4-dihydro-3H-pyrazol-3-one(3) (17.4 g, 0.1 mol) was added slowly and the reaction mixture was stirred for a further period of 15–20 min. Then the contents were heated at 70 °C for 10 h. The reaction progress was monitored using TLC. After completion of the reaction, the contents are poured into crushed ice with continuous stirring. Solid mass separated was filtered, washed with water, dried and recrystalised from ethanol. m.p: 135 °C [34] (135–145 °C), Yield 82 %.

Synthesis of 5-(2,4-dichlorophenoxy)-3-methyl-1-phenyl-1H-pyrazole-4-carbaldehyde (5)

2,4-dichloro phenol (0.1 mol) was dissolved in 20 ml of dimethyl sulfoxide, 5-chloro-3-methyl-1-phenyl-1H-pyrazole-4-carbaldehyde (4) (22 g, 0.1 mol) and potassium hydroxide (5.6 g, 0.1 mol) were added and the reaction mixture was then heated on an oil bath at 60 °C for 6 h. The reaction mixture was cooled to room temperature and poured into crushed ice. The solid separated was filtered and washed with water and dried. The product was further purified by recrystallization from ethanol. m.p 99 °C [35-37] 99–101 °C). Yield 81 %.

Synthesis of 4-(((5-(2,4-dichlorophenoxy)-3-methyl-1-phenyl-1H-pyrazol-4-yl)methylene)amino)-5-propyl-4H-1,2,4-triazole-3-thione (7c)

An equimolar quantities of 5-(2,4-dichlorophenoxy)—3-methyl-1-phenyl-1H-pyrazole-4-carbaldehyde (5) and 4-amino-5-propyl-4H-1,2,4-triazole-3-thiol ((6) [37,15,16] taken in ethanol(20 ml) in an R. B. Flask added few drops of acetic acid and refluxed for 6 hrs on a water bath. The completion of the reaction was monitored by TLC. The resultant mixture was cooled to room temperature, the solid separated was filtered and dried and recrystallization from ethanol (Scheme 1).

FT-IR (**KBr cm**⁻¹): N—H (3093), C—H (2927), S-H (2848), C=N (1597), C=C(1485), C—N (1310), C—O (1284), C=S (1199), C-S (752).

¹H NMR (400 MHz, DMSO-d6)δ ppm: 0.86 (t, 3H, CH₃ of propyl), 1.53 (m, 2H, CH₂ of propyl), 2.34 (t, 2H, CH₂ of propyl), 2.50 (s, 3H, CH₃ of pyrazole), 7.06 (d, 1H, J=8.8 Hz, 6-H of 2,4-dichlorophenyl), 7.38 (dd, 1H, J=8.8 Hz& 2.4 Hz, 5-H of 2,4-dichlorophenyl), 7.38 (d, 1H J=2 Hz, 3-H of 2,4-dichlorophenyl), 7.40 – 7.74 (m, 5H, Ar-H), 10.02 (s, 1H, N=CH), 13.71 (s, 1H, SH).

LC-MS: m/z: 487 (M⁺ + 1), 489 (M⁺ + 3), 489 (M⁺ + 5) Chlorine isotope, M.F: (C₂₂H₂₀Cl₂N₆OS), M.P: (165 °C), Yield 71 %.

3. Methodology

3.1. X-ray crystallography

A translucent pale colourless block-like single crystal of compound 7c with approximate dimensions of $0.4\times0.3\times0.2$ mm was chosen for single crystal X-ray diffraction study. The X-ray intensity data were measured at 296 K ($\lambda=0.71073$ Å). The total exposure time was 3 h. The frames were integrated with the Bruker SAINT software package [38] using a narrow-frame algorithm. The integration of the data using a triclinic unit cell yielded a total of 13,746 reflections to a maximum 0 angle of 28.453°. (0.75 Å resolution). The final cell constants and volume below are based upon the refinement of the XYZ-centroids of 5548 reflections above $2\sigma(I)$ with 2.644 $^{\circ}$ < 0 < 28.453°.

3.2. Hirshfeld surface analysis

Hirshfeld surface analysis was carried out to explore the intermolecular interactions which are responsible for molecular packing in the crystal. The molecular surfaces which are required for this analysis were generated by employing CrystalExplorer17.5 [39]. These surface contain the detailed information about all the interactions simultaneously which are responsible for molecular packing in a crystal. For each point on the surface, two distances d_i and d_e were the first functions of distance (explored) defined for the mapping on the Hirshfeld surface; where d_i and d_e are the distances from the points on the Hirshfeld surface

to the nearest nucleus internal and external to the surface respectively [40].

3.3. DFT calculations

DFT calculations are helpful in studying the various properties, viz., geometry, energy, electronic excitations, frontier molecular orbitals, spectroscopic properties, etc. The density functional theory (DFT) calculations were performed using Gaussian software [41]. The molecular geometry optimization was carried out using Hartree-Fock (HF), B3LYP hybrid functions with 6-31+G(d, p) as basis set.

3.4. Noncovalent interaction study

To explore the weak interactions present in the molecule, quantum theory of atoms in molecules (QTAIM) and reduced density gradient (RDG) analysis were carried out. *Multiwfn 3.8* [42] was used for the noncovalent interaction studies and were visualized by *Visual Molecular Dynamics* [43]. Molecular electron densities, and electrostatic potential maps provide the reactive site and charge distribution of the compound.

3.5. Molecular docking

Molecular docking has become the most important component of the design and discovery of novel drugs. Molecular docking studies play a vital role in the understanding of various biological processes and to design a drug for the cause. *In silico* docking studies were carried out for the compound **7c** to understand the molecular interactions involved between the active binding sites of the compound against the main protease of *SARS-Covid-2* (Mpro) by employing an AutoDock software [44].

In molecular docking, the binding mode with the lowest energy score is predicted as the best match. The energy minimization was done using the default parameters to achieve the best possible outcome. The molecular docking analysis was closely investigated for the best docking scores and protein ligand interactions.

The protein structures (PDB ID:6LU7 and 7K40) were downloaded from the protein data bank https://www.rcsb.org/. Solvating water molecules and the co-crystallized native ligand along with hetero atoms were removed. The ligand molecules in PDB format were loaded using AutoDock Tool's ligand menu. The ligand and receptor were then saved in pdbqt format respectively. Docking was done using AutoDock. The binding sites were defined using the grid box with an energy range of 4. Each aminoacid's value is defined by its Kollman charges generated from the associated electrostatic potential and the polar hydrogen atoms were added to the protein [45,46]. Lamarckian algorithm was employed to dock the protein. The docking calculations were performed using default parameters and 50 docked conformations were generated for the compound. Graphics of protein ligand binding sites are obtained from and Schrodinger maestro [47] and Biovia Discovery Studio visualizer 22 software.

3.6. Molecular dynamics

The molecular dynamics (MD) simulations have become an essential approach in understanding stability, binding affinity of the complex with the protein. It is very essential to understand the structure-function relationship of the target molecule in the field of molecular biology and drug discovery. To find the stability and binding affinity of the compound 7c, MD simulations were performed using schrodinger maestro [academic version 2020.4] on linux platform for the best hit docked protein–ligand complex. MD trajectory graphs of docked complexes were analyzed to get RMSD (Root Mean Square Deviation) and RMSF (Root Mean Square Fluctuation).

Table 1
Crystal data and structure refinement details for the compound 7c.

CCDC number	2266397
Empirical formula	C ₂₂ H ₂₀ Cl ₂ N ₆ O S
Temperature	296 K
Wavelength	0.71073 Å
θ range	2.64° to 28.45°
Crystal system	Triclinic
Space group	P-1
Cell parameters	a = 7.4037(7) Å,
	b = 11.4459(10) Å,
	c = 15.0486(12) Å,
	$\alpha = 73.850(4)^{\circ}$,
	$\beta = 80.513(4)^{\circ}$,
	$\gamma = 73.487(4)^{\circ}$
Volume	1169.30(18)Å ³
Z	2
Density(calculated)	1.384 Mg m $^{-3}$
Absorption coefficient	0.394 mm $^{-1}$
F_{000}	504
Crystal size	$0.4\times0.3\times0.2~mm$
Index ranges	$-9-\leq h\leq 9$
	$-15 \le k \le 15$
	$-20 \le l \le 20$
Reflections collected	13746
Independent reflections	5548 [$R_{\text{int}} = 0.0332$]
Absorption correction	Multi-scan
Refinement method	Full matrix least-squares on F^2
Data / restraints /parameters	5548 / 1 / 295
Goodness-of-fit	0.987
Final $[I > 2\sigma(I)]$	$R_1=0.0465,wR_2=0.1123$
R indices (all data)	$R_1 = 0.0810, wR_2 = 0.1340$
Largest diff. peak and hole	$0.259 \text{ and } -0.233 \text{ e Å}^{-3}$

Table 2Selected bond lengths of the compound **7c**.

Atoms	Length (Å)		Atoms	Length (Å)	
	XRD	DFT		XRD	DFT
C(1)-C(6)	1.371(3)	1.395	C(7)-C(8)	1.482(3)	1.495
C(1)-C(2)	1.388(3)	1.393	C(9)-C(11)	1.374(3)	1.394
C(2)-C(3)	1.370(4)	1.393	C(9)-C(10)	1.435(3)	1.441
C(3)-C(4)	1.364(4)	1.394	C(10)-N(4)	1.272(3)	1.289
C(4)-C(5)	1.379(3)	1.391	C(11)-O(1)	1.347(2)	1.350
C(5)-C(6)	1.380(3)	1.396	C(11)-N(5)	1.348(2)	1.358
C(6)-N(5)	1.427(2)	1.427	C(12)-C(17)	1.374(3)	1.391
C(7)-N(6)	1.316(3)	1.322	C(12)-C(13)	1.380(3)	1.398

Table 3 Selected bond angles of the compound **7c**.

Atoms	Bond angle (°)	
	XRD	DFT
C(6)-C(1)-C(2)	119.4(2)	119.4
C(3)-C(2)-C(1)	120.4(3)	120.5
C(4)-C(3)-C(2)	119.7(2)	119.7
C(3)-C(4)-C(5)	120.9(2)	120.4
C(4)-C(5)-C(6)	119.2(2)	119.5
C(1)-C(6)-C(5)	120.4(2)	120.6
C(1)-C(6)-N(5)	120.9(2)	120.9
C(5)-C(6)-N(5)	118.7(2)	118.5
N(6)-C(7)-C(9)	111.5(2)	111.5
N(6)-C(7)-C(8)	121.1(2)	120.6

4. Results and discussions

4.1. X-ray crystallography

Crystal structure was solved by the direct methods using SHELXS program. All the non-hydrogen atoms were refined anisotropically against F^2 using SHELXL [48] program. The hydrogen atoms were

Table 4Selected torsion angles of the compound 7c.

Atoms	Torsion angle (°)		
	XRD	DFT	
C(6)-C(1)-C(2)-C(3)	1.4(3)	0.80	
C(1)-C(2)-C(3)-C(4)	0.2(4)	0.04	
C(2)-C(3)-C(4)-C(5)	-1.3(4)	-0.64	
C(2)-C(1)-C(6)-N(5)	179.6(2)	-179.8	
C(5)-C(6)-N(5)-C(11)	145.6(2)	139.2	
C(1)-C(6)-N(5)-N(6)	152.1(2)	142.5	
C(5)-C(6)-N(5)-N(6)	-26.5(3)	-36.37	
C(9)-C(11)-O(1)-C(12)	-71.5(3)	-70.28	
C(11)-N(5)-N(6)-C(7)	0.3(2)	0.92	

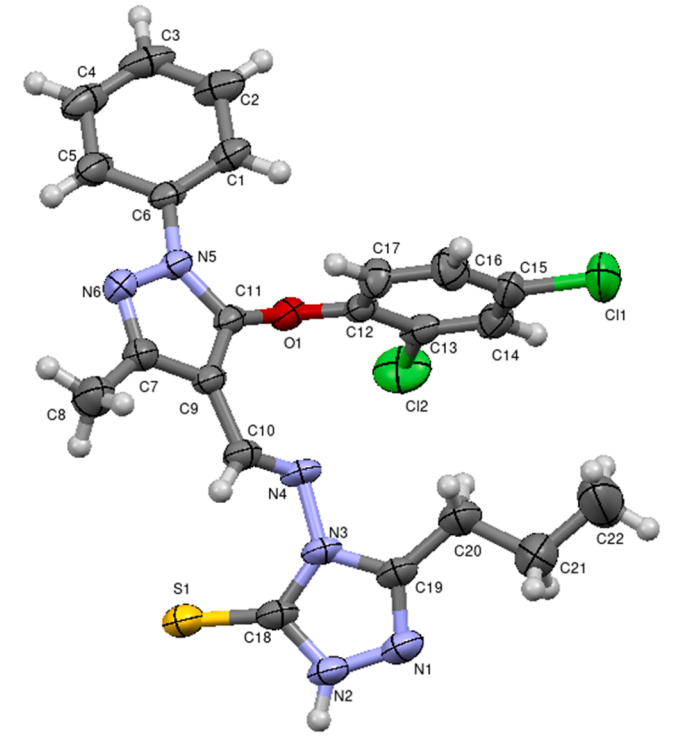


Fig. 1. The ORTEP of the compound 7c with 50 % probability ellipsoids.

placed in geometrically ideal positions and allowed to ride on their parent atoms.

A total of 295 parameters were refined with 55,488 unique reflections. After the final refinement, the residual factor *R* converged to 0.0465. Geometrical calculations were performed using *PLATON* [49]. *MERCURY* [50] software was employed to generate *ORTEP* and packing diagrams. A summary of the crystal structure data and refinement details for the compound **7c** are listed in Table 1. Selected bond lengths, a few bond angles and torsion angles obtained from the XRD data for the compound **7c** are listed in Table 2, Table 3, and Table 4 respectively.

The compound **7c** crystallizes in the triclinic system in the space group $P1^-$. The *ORTEP* of the compound is shown in Fig. 1. All the rings in the structure are sp^2 hybridized. Both phenyl and triazole rings are in planar conformation with the central pyrazole ring as evident by the torsion angle values of C(2)-C(1)-C(6)-N(5) = 179.65(19)°, C(4)-C(5)-C (6)-N(5) = 179.3(2)°, C(6)-N(5)-N(6)-C(7) = 173.80(18)°, C(9)-C(10)-N (4)-N(3) = $-175.32(18)^\circ$, and C(11)-C(9)-C(10)-N(4) = $3.6(3)^\circ$.

The dichlorophenoxy ring is essentially planar with a maximum r.m. s. deviation of 0.008(2) Å for C12 atom. It is observed from the torsion angle value (S1-C18-N2-N1 = 176.18(18)°) that the thione group is in antiperiplanar conformation with the triazole ring.

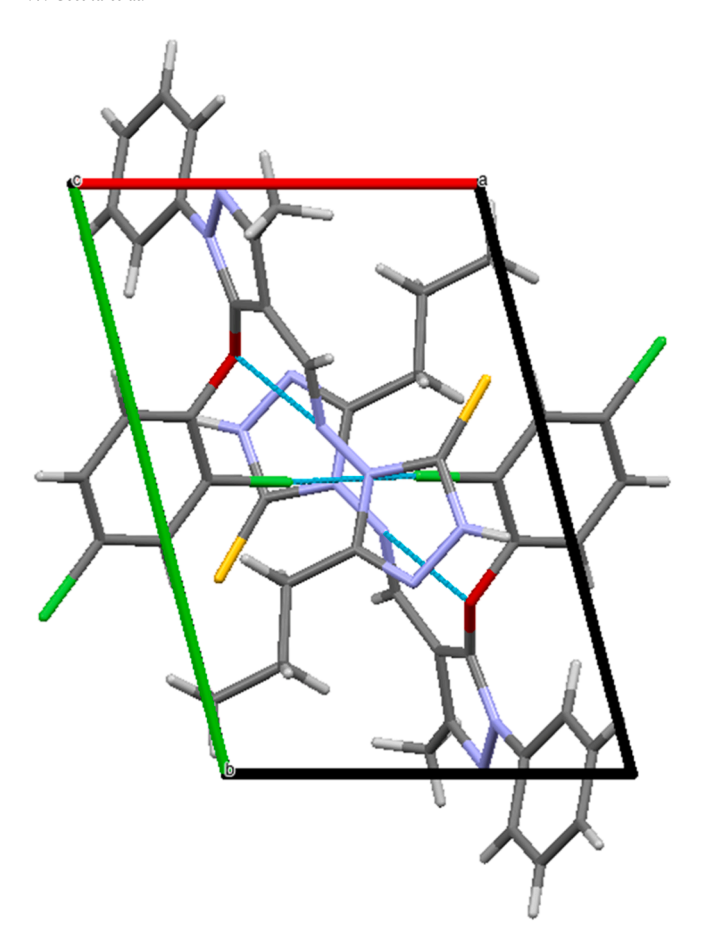


Fig. 2. Packing of the molecules when viewed along c axis.

Table 5 Hydrogen bond geometry.

D-HA	D-H (Å)	HA (Å)	DA (Å)	D-HA (°)
N2-H2NS1 ^a	0.87	2.45	3.113(3)	173
C1-H1O1	0.93	2.48	2.954(3)	112
C10-H10S1	0.93	2.87	3.249(3)	106
C10-H10N1 ^b	0.93	2.61	3.378(3)	140

Note: a and b indicate the intermolecular interactions with symmetry codes 2-x, 1-y, -z and 1-x, 1-y, -z respectively.

4.2. Molecular packing and hydrogen bond analysis

Packing of the molecules when viewed along c axis is shown in Fig. 2. The molecular structure exhibits various *Cg-Cg* and C—H...Cg interactions, which help to stabilize the crystal structure. Various hydrogen bond interactions along with the geometry details are listed in Table 5. In the crystal structure, the intramolecular hydrogen bond interactions C1-H1...O1 and C10-H10...S1 are observed. Also, the crystal structure is characterized by N2-H2N..S1 and C10-H10...N1 intermolecular interactions, which helps to form the supramolecular assembly.

4.3. Hirshfeld surface analysis

Fig. 3 highlights the Hirshfeld surface mapped over $d_{\rm norm}$. The bright red regions on the surface are from N—H...O and S-H...O contacts. The red regions arise from those interactions which are shorter than van der Waals radii with negative $d_{\rm norm}$ value; blue regions on the surface are from interactions which are longer than van der Waals radii with positive $d_{\rm norm}$ value; whereas white regions are from neutral contacts with zero $d_{\rm norm}$ value [51]. Fig. 4 displays the associated fingerprint plots of

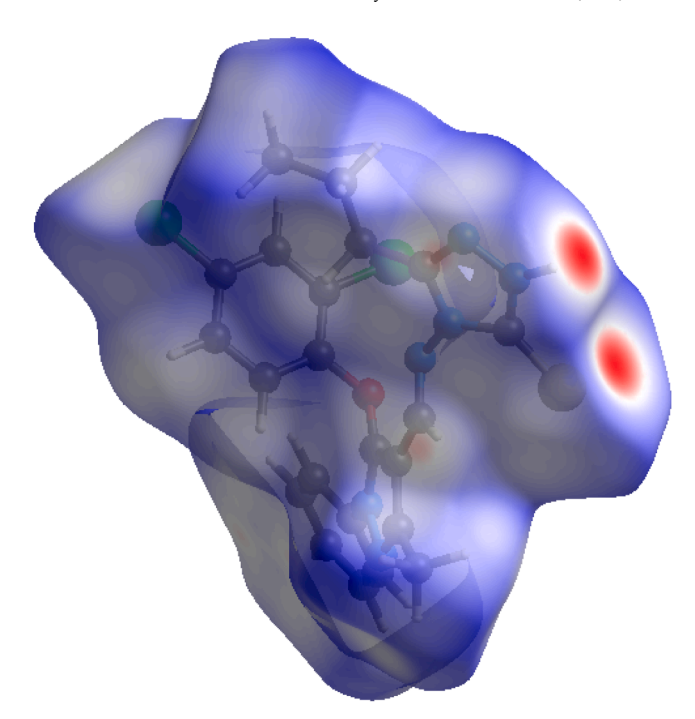


Fig. 3. Hirshfeld surface mapped over d_{norm} .

the compound. The $d_{\rm i}$ and $d_{\rm e}$ on the plot are the distances from the Hirshfeld surface to the nearest nuclei inside and outside the surface respectively. For any given $d_{\rm i}$ and $d_{\rm e}$ pairs, white color shows no occurrence, blue color some occurrence, and green indicates more frequent occurrence. These plots give the percentage contribution of each contact to the total Hirshfeld surface area. The major contribution to the total Hirshfeld area are from H—H contacts which is about 40.3 %. The remaining significant contributions are from N—H (11.3 %), S-H (11.1 %), Cl-H (10.9 %), C—H (9.4 %), O—H (2.7 %). The extended symmetrical 'spikes' in the Fig. 4(a) are the characteristics of S-H intermolecular hydrogen bond interactions.

4.4. DFT calculations

Experimentally derived geometrical parameters viz., bond lengths, bond angles, and torsion angles obtained by the single crystal X-ray diffraction method and theoretically computed geometrical parameters are found to be in good agreement with certain deviations (root mean square deviation (RMSD) of 1.751 Å) and they are tabulated in the Tables 2, 3, and 4. The deviations observed could be related to DFT calculations are performed in the gaseous phase whereas XRD results are from condensed solid state, The optimized structure and structural overlay are shown in Figs. 5a and 5b respectively.

The frontier molecular orbitals HOMO (highest occupied molecular orbital) and LUMO (lowest unoccupied molecular orbital) were generated. The molecular orbital energies and their energy gap for the title compound were studied. The energy gap between the molecular orbitals plays a vital role in the kinetic stability of the molecule, as well as intermolecular charge transfer interactions. A large value of energy gap between the molecular orbitals is associated with the high kinetic stability [52]. If the energy gap between HOMO and LUMO is small, the molecule will be more reactive [51]. The distribution of molecular orbitals HOMO, HOMO-1, LUMO, and LUMO+1 levels, and their energy gaps computed with B3LYP/6–311+G(d, p) basis set for the compound are shown in Fig. 6. The estimated energy gap between the HOMO and LUMO levels is 3.824 eV.

The HOMO is completely localized in the triazole ring, whereas the LUMO is localized in the pyrazole and phenyl ring. The larger gap between HOMO and LUMO (3.824 eV) accounts for the stability in the

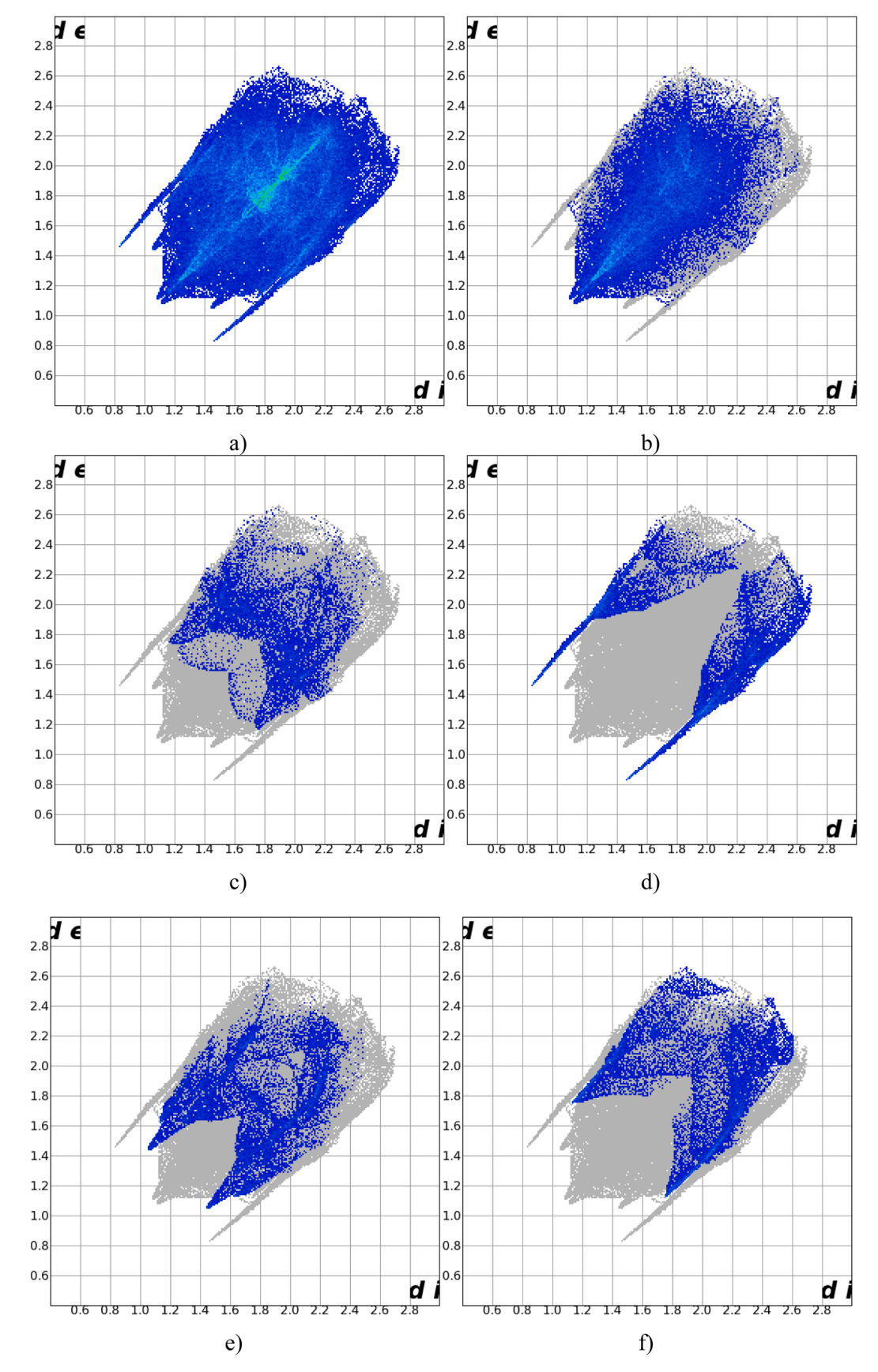
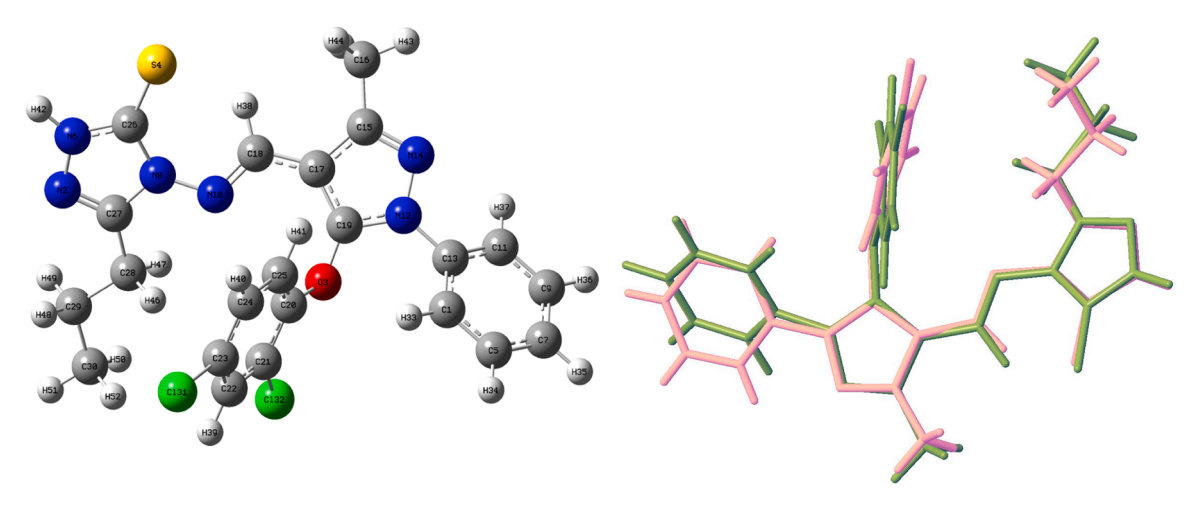
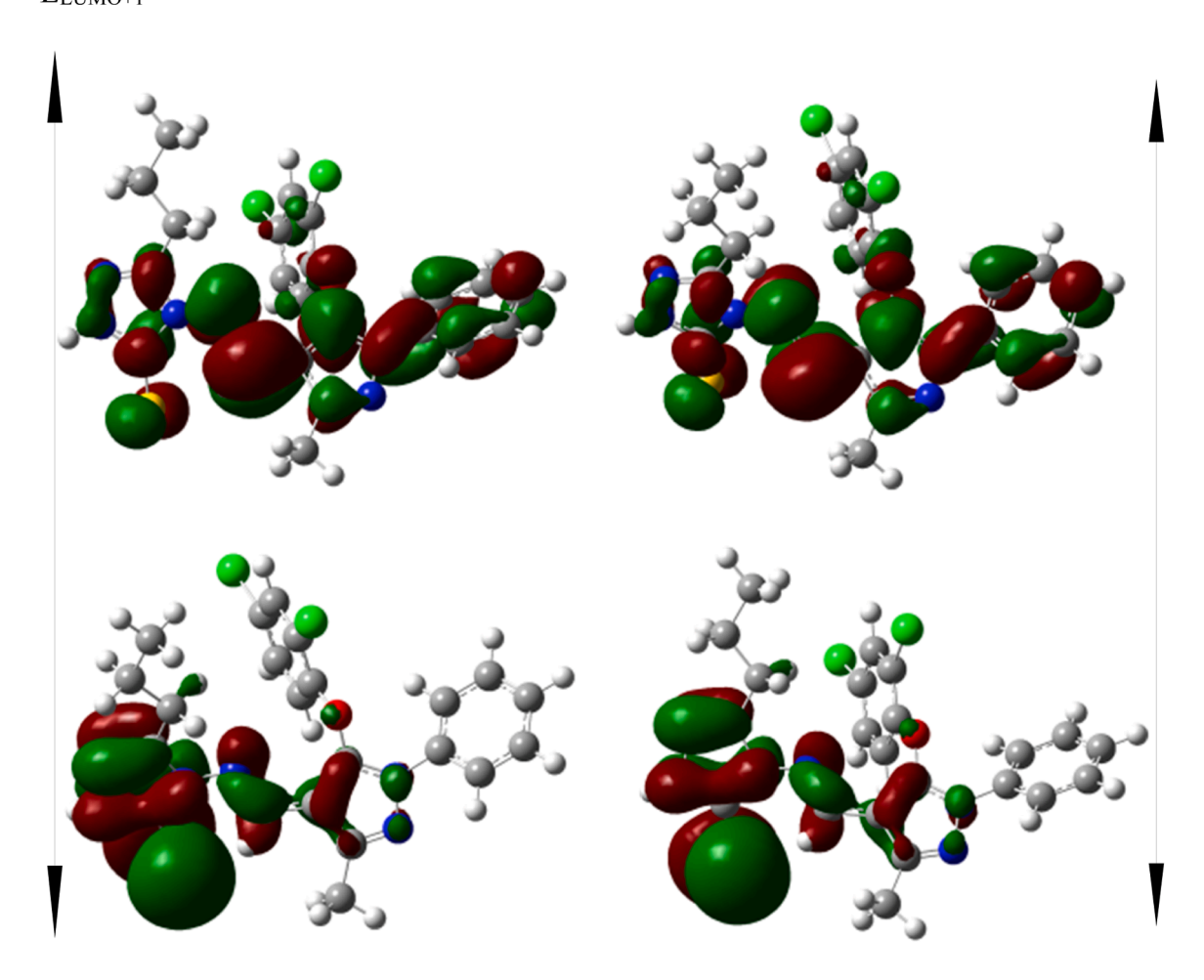


Fig. 4. Fingerprint plots of the compound a) From all the contacts and Decomposed fingerprint plot showing b) H—H contacts, c) C—H contacts,d) S-H contacts, e) N—H contacts, f) Cl-H contacts.



 $Fig. \ 5. \ a) \ \text{The optimized structure and} \ b) \ \text{The superposition of two structures of the compound} \ 7c \ (\text{Green (XRD)}, \ \text{Pink (DFT)}).$

 $\begin{array}{c} E_{LUMO} \\ E_{LUMO+1} \end{array}$



E_{HOMO-1}

Fig. 6. HOMO, LUMO, HOMO-1, LUMO+1 energy levels.

Table 6Calculated energy values and quantum molecular descriptors for the compound **7c**.

Parameters	Values
Еномо	−5.841 eV
E _{LUMO}	-2.017 eV
$\Delta \mathrm{E}$	3.824 eV
Ionization potential (I)	5.841 eV
Electron affinity (A)	2.017 eV
Electronegativity (χ)	-3.929 eV
Chemical potential (µ)	3.929 eV
Chemical hardness (η)	1.912 eV
Global softness (σ)	0.523 eV^{-1}
Electrophilicity (ω)	4.036 eV

solid state of the compound studied. Table 6 lists the ionization potential, the electron affinity, electronegativity, global softness, global hardness, global electrophilicity, and the chemical potential for the compound.

4.5. Non covalent interaction study

The covalent bond is mainly responsible for three dimensional structure of the molecule. Along with the covalent bond, non-covalent interactions play a major part in the bonding of molecules. Thus, the non-covalent interaction study has a good significance. Electron density and its derivatives furnish the information on the nature and type of interaction. Firstly, the interaction in the compound 7c is analysed by reduced density gradient (RDG). The weak interactions correspond to the low gradient region. Also, the positive value of Laplacian of the electron density is an indicator of weak interaction. The 2D scattered plot of RDG versus $sign(\lambda_2)\rho$ visualizes the type of interaction. From the scattered plot, one can distinguish H-bonding, van der Waals, and steric interactions based on the spikes corresponding to $sign(\lambda_2)\rho$ value. The region is partitioned as negative $sign(\lambda_2)\rho$ to positive $sign(\lambda_2)\rho$ value conceived as strong attraction to strong repulsion [53].

In the studied molecule, the spikes on the scattered plot (Fig. 7) with values less than zero belong to the weak interaction. Also, we can observe that positive value of $sign(\lambda_2)\rho$ near zero are the indicator of van der waals interaction. There are spikes with large positive $sign(\lambda_2)\rho$

value belonging to steric repulsion. The NCI plot with isosurfaces in blue-green-red also picturize the interactions in the molecule. Red isosurfaces inside the rings have appeared due to the steric repulsion between atoms in the ring. The presence of the weak interactions are shown in green isosurfaces.

The weak interactions are also brought to light by quantum theory of atoms in molecule (QTAIM) analysis. The bond critical path (BCP) generated between non-bonded atoms is evidence for the interaction in the molecule. In the Fig. 8, the BCP generated between donor (C—H) and acceptor atom S and donor (C—H) and acceptor atom O indicates the intramolecular interaction. The obtained topological parameters, the electron density, and Laplacian $\nabla^2\rho$ at BCP's clearly specify the nature of the interaction. Small values of ρ and positive $\nabla^2\rho$ corresponds to the (van der Waals or hydrogen bond) non-covalent interaction [54]. From the Table 7, one can infer that the BCP's positive values of $\nabla^2\rho$ signify the presence of hydrogen bond. The ratio of $G(r)_{BCP}$ and $V(r)_{BCP}$ being greater than 1 and E_{HB} value less than 12.0 kcal/mol implies that the hydrogen bond is weak in nature.

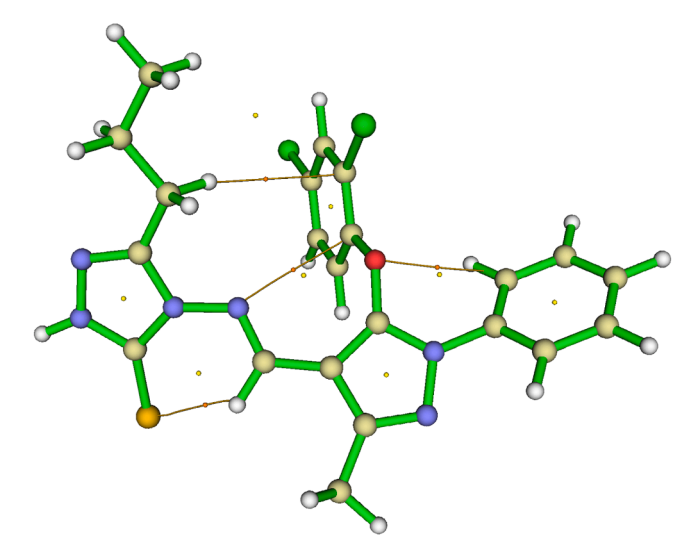
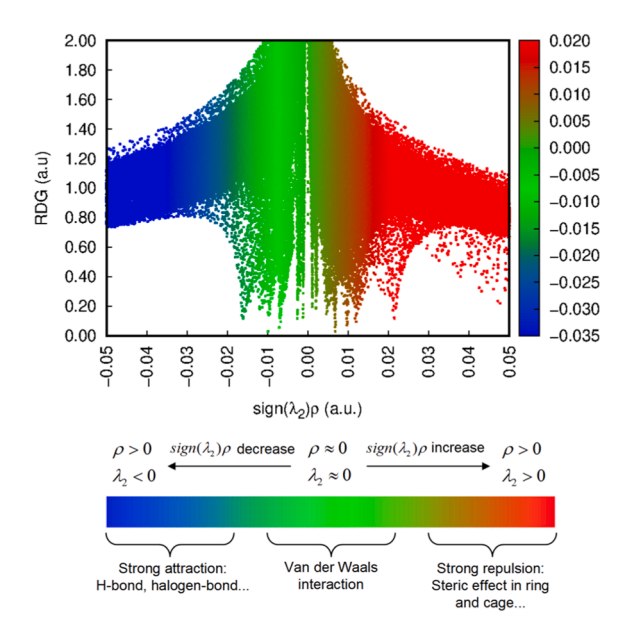
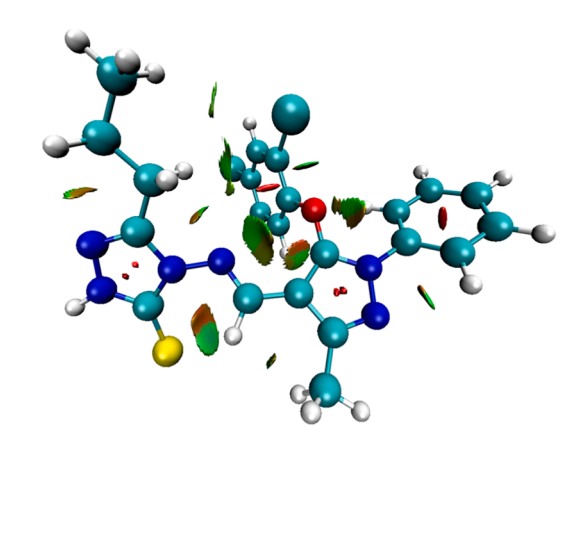


Fig. 8. Molecule with intramolecular interactions from QTAIM calculations.



 \mathbf{a}



b

Fig. 7. a) 2D scattered plot and b) RDG isosurface.

Table 7Topological parameters of bonds obtained from AIM analysis.

Interaction X-H···Y	ρ _{BCP} (a.u)	$\nabla^2 \rho_{BCP}$ (a.u)	G(r) _{BCP} (a.u)	V(r) _{BCP} (a.u)	E _{HB} kcal/ mol	-G (r) _{BCP} / V(r)
C10-	0.0164	0.0472	0.0105	-0.0091	-2.91	1.15
H10···S1 C1-H1···O1	0.0098	0.0380	0.0081	-0.0067	-1.44	1.20

4.6. Molecular electrostatic potential

The electrostatic potential arises due to the total charge distribution in the molecule, and it can be visualized on the molecular electrostatic map (MEP). The MEP map represents the electrophilic and nucleophilic regions in the molecule. Fig. 9 shows the molecular electrostatic potential for the compound 7c. The potential value ranges from -27.65 kcal/mol to 44.97 kcal/mol. The electrophilic regions are mapped in red color and nucleophilic regions are mapped in blue colour. The red regions around the sulphur atom attached to triazole group, nitrogen atom of triazole and pyrazole groups and blue regions around the hydrogen atom of triazole group indicate the excellent reactive sites of donor and acceptor atoms in the molecule [55].

4.7. Molecular docking: analyses of protein-ligand binding interactions

Molecular docking is a powerful tool to investigate and to understand the ligand receptor binding interactions, which is helpful for the design of new potential drugs. We have investigated ligand-protein binding interactions for *SARS-CoV-2* main protease. A two-dimensional diagram of the receptor-ligand interactions in the molecule is generated to show the active interactions. Fig. 10 shows the molecular docking conformations with target protein.

Based on the docking score, compounds are chosen as good drug compounds. The docking score signifies the strength of the receptor ligand interactions. For the studied compound 7c, a docking score of -10.43 kcal/mol for 6LU7 protein was the most active ligand compared to 7K40 whose binding score was -8.94 kcal/mol. Fig. 11 depicts the 2D representation of the protein-ligand interaction with residues.

Out of 11 amino acid residues in the active site of the main protease 6LU7, the ligand formed a single hydrogen bond interaction with amino acid residue CYS145 (for triazole group), seven alkyl interactions, with TYR54, MET49, HIS163 (for phenyl group), and HIS163, PRO52, CYS44, MET165 (for methyl group). One π -carbon interaction with HIS41 (for dichlorophenoxy group) and three π -alkyl interactions with HIS164, HIS41, MET165 (for dichlophenoxy group and phenyl group) were also found (Fig. 11a).

Out of 13 amino acid residues in the active site of the main protease 7K40, the ligand formed two hydrogen bond interactions with amino acid residues HIS163, PHE140 (for the Sulphur atom), three hydrogen bond interaction interactions with amino acid residues SER144, LEU141, and GLY143 (for triazole group), three alkyl interactions with HIS41, ASN142, and MET49 (for dichlorophenoxy group). In addition to these interactions, phenyl group of the compound **7c** exhibits n-sigma interaction with MET165 amino acid residue (Fig. 11b).

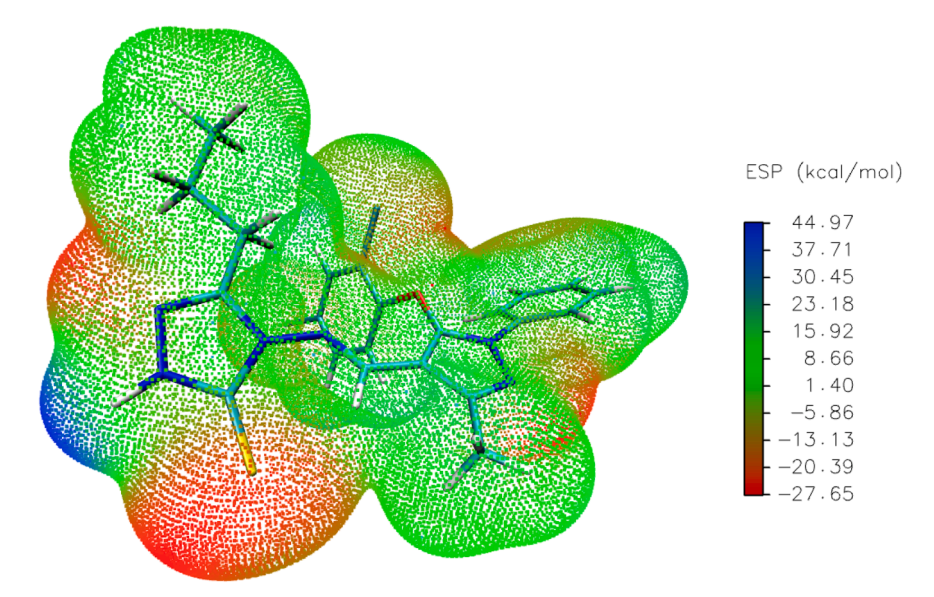


Fig. 9. Molecular electrostatic potential for the compound 7c.

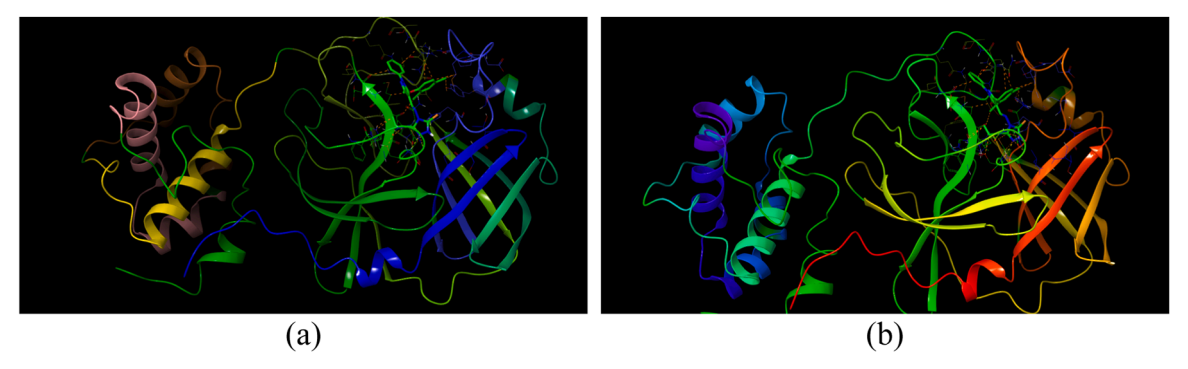


Fig. 10. Molecular docking conformations for protein-ligand interaction (a) 6LU7 and (b) 7K40.

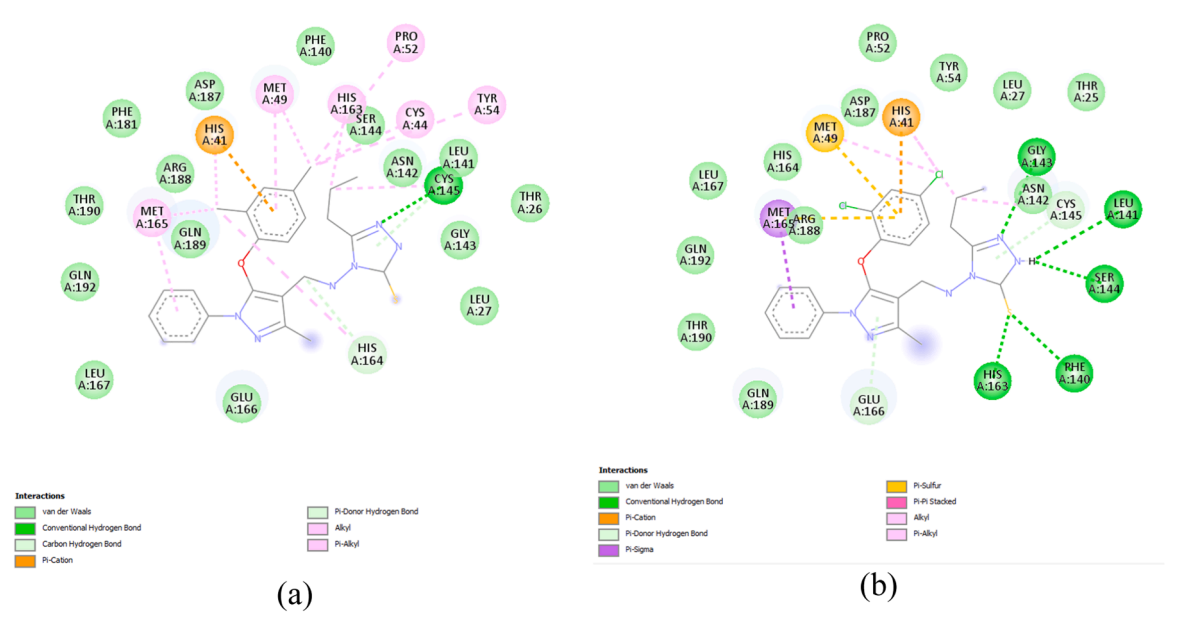


Fig. 11. 2D representation of molecular docking interactions with protein-ligand residue (a) 6LU7 and (b) 7K40.

Table 8
Molecular docking results of standard drug (Remdesivir).

Protein	Docking score (kcal/mol)	Docking conformations	Amino acids
6LU7	-3.31		GLY:138, GLY:170, LYS:137, GLN:127, GLU:290, LYS:5
7K40	-7.63		MET:49,MET:165,ASP:187,HIS:41,HIS:164,CYS:145,GLU:166,PHE:140, LEU:167,PRO:168

Further, docking conformations of the compound **7c** were compared with the standard drug Remdesivir [56]. The binding scores, docking conformations and 2D interactions are listed in Table 8. The studied compound **7c** shows better results compared to standard drug.

4.8. Molecular dynamics simulation: RMSD and RMSF analysis

To understand the stability of the protein-ligand complex, the molecular dynamics (MD) simulations were carried out for the compound 7c for 100 ns. MD results were analyzed to get RMSD and RMSF. The RMSD represents an average deviation in the protein-ligand complex from its initial pose with respect to time. Figs. 12A and 12B demonstrate RMSD plots of compound 7c with 6LU7 and 7K40 proteins respectively. For the docked 6LU7-ligand complex, the RMSD plot of protein-ligand complex has remained stable with considerable deviations until 40 ns.

But thereafter, the RMSD value did not vary significantly, the ligand stays well within the binding pocket, which remains nearly constant until the end of the simulation period (100 ns). Whereas for 7K40-ligand complex, the RMSD value shows major differences until 22 ns and in the range of 80-100 ns, the plot remains stable during the period of 22ns-80 ns.

RMSF is a measure of individual residue flexibility, i.e., how much a particular residue fluctuates during a simulation [57]. The peaks in the RMSF plot indicates the residues with the greatest oscillation during simulation [58]. Figs. 13A and 13B depict the RMSF graph of compound 7c with 6LU7 and 7K40 proteins respectively.

5. Conclusion

In the present study, a novel series of hydrazones were synthesized

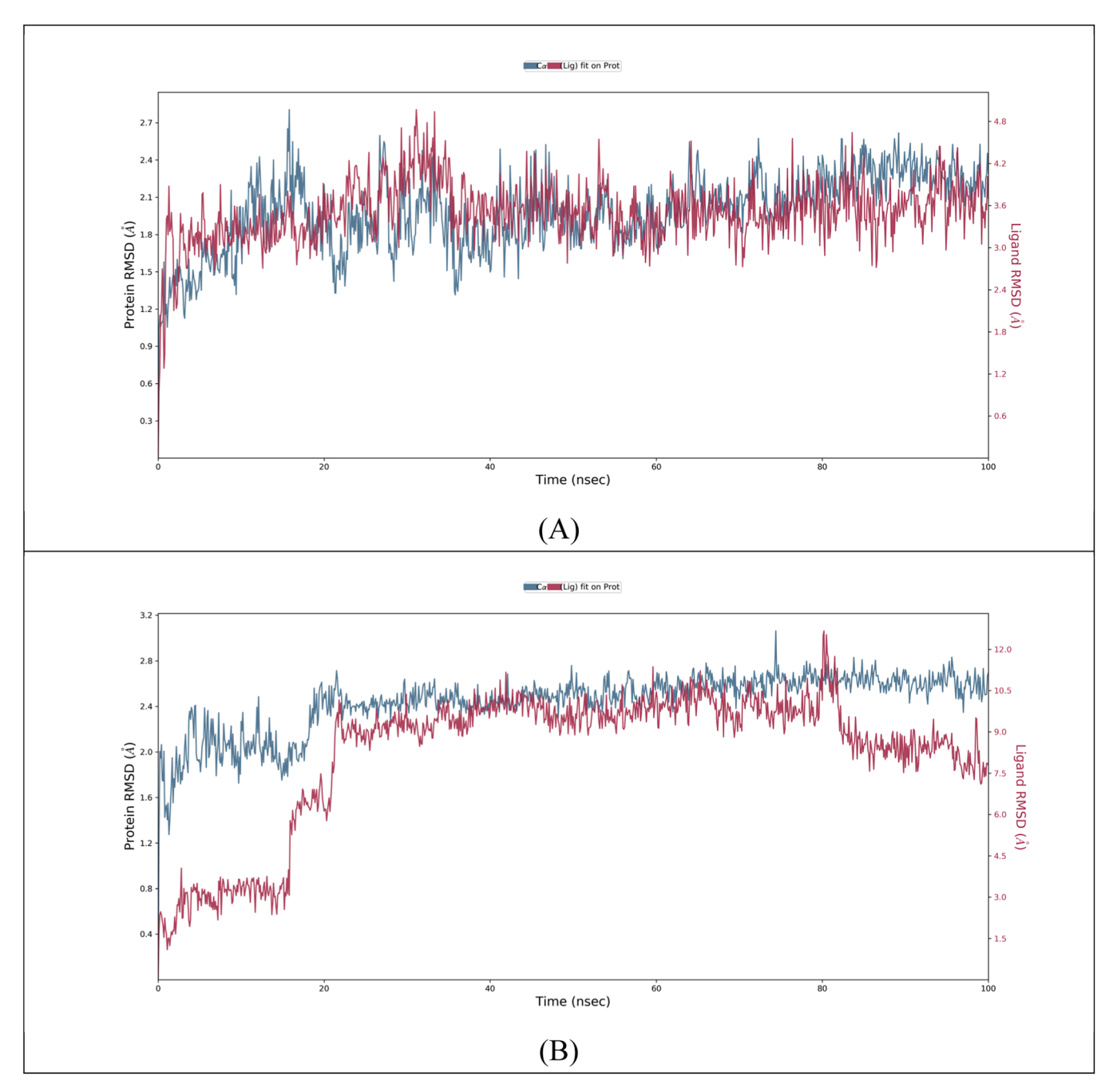


Fig. 12. The RMSD graph of compound 7c with (A) 6LU7 protein (B) 7K40 protein.

and characterized using spectroscopic techniques FTIR, 1 HNMR, and single crystal XRD. The crystal structure was confirmed by single crystal X-ray diffraction studies. It was found that the final compound has been crystallized in a triclinic crystal system in the space group $P1^-$. The Hirshfeld surface analysis was carried out to understand the various intermolecular interactions present in the crystal structure. DFT calculations were performed to correlate with the experimental data and it was found that the results were in good agreement with the experimental XRD data. The study of frontier molecular orbitals revealed that, the energy gap between the HOMO and LUMO levels is 3.824 eV, which accounts for high stability of the molecule. Molecular docking studies revealed that the compound 7c showed a good binding score with Mpro protease 6LU7 compared to 7K40 protease. Further molecular dynamics simulations were performed for the best hit docked complexes to understand the stability and binding affinity of the protein-ligand

complexes.

CRediT authorship contribution statement

D.V. Geetha: Writing – original draft. C.L. Sharath: Conceptualization.
 N. Shivakumar: Methodology.
 B.N. Lakshminarayana: Writing – review & editing, Supervision. K.M. Chandini: Visualization. K. Balakrishna: Supervision.

Declaration of competing interest

The authors declare that they have no known competing financial interests or personal relationships that could have appeared to influence the work reported in this paper.

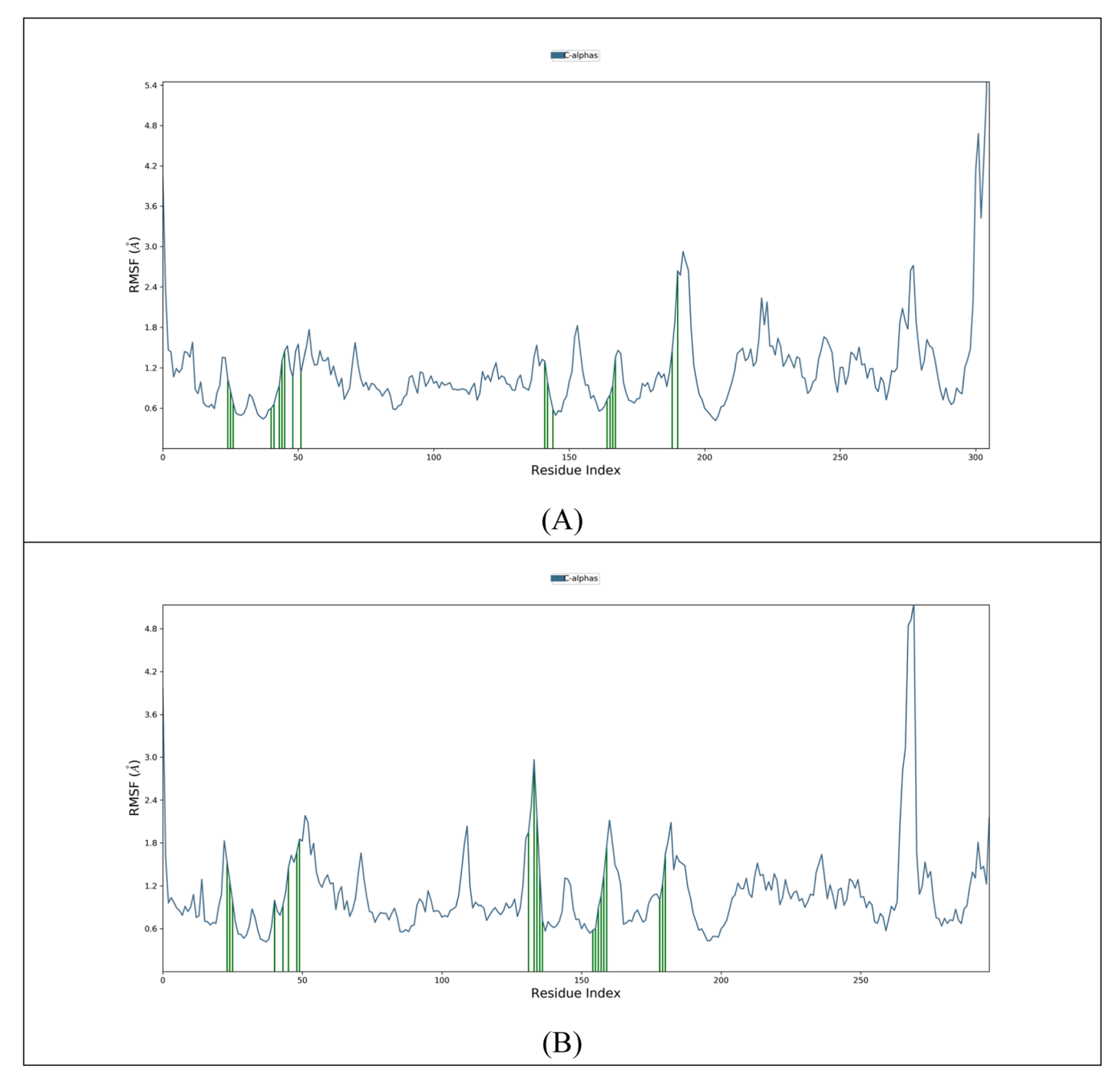


Fig. 13. The RMSF graph of compound 7c with (A) 6LU7 protein and (B) with 7K40 protein.

Data availability

Data will be made available on request.

Supplementary materials

Supplementary material associated with this article can be found, in the online version, at doi:10.1016/j.molstruc.2024.139016.

References

- [1] M.M. Ismail Othman, M.A.M. Gad-Elkareem, Abd El-Galil E. Amr, M.A. Al-Omar, E. S. Nossier, E.A. Elsayed, J. Enzyme Inhib. Med. Chem. 35 (1) (2020) 1491–1502.
- [2] A. Sheena Mohan, A. Asha, S. suma, M.R. Sudarsanakumar, M.R. Prathapchandra kurup, J. Indian Chem. Soc. 97 (11a) (2020) 2274–2281.

- [3] P. Raghurama Shetty, G. Shivaraja, G. Krishnaswamy, K. Pruthviraj, Vivek Chandra Mohan, S. Sreenivasa, Indian J. Heterocyclic Chem. 30 (2) (2020) 123–130.
- [4] M.M.M. El-Miligya, A.K. Al-Kubeisib, M.G. Bekhitc, Saad R. El-Zemityd, Rasha A. Nassrae, Aly A. Hazzaaa, J. Enzyme Inhib. Med. Chem. 38 (1) (2023), 2914-308.
- [5] B.S. Holla, B. Kalluraya, K.R. Sridhar, Curr. Sci. 56 (5) (1987) 236–238.
- [6] A.A. Bekhit, S.N. Nasralla, E.J. El-Agroudy, N. Hamouda, A. Abd El-Fattah, Sa A. Bekhit, K. Amagase, T.M. Ibrahim, Eur. J. Pharm Sci. 168 (2022) 106080.
- [7] C. Brullo, E. Russo, S. Garibaldi, P. Altieri, P. Ameri, S. Ravera, M.G. Signorello, Antioxidants 2 (2023) 2.
- [8] J.C. Hegde, K.S. Girish, B.Kalluraya A.Adhikari, Eur. J. Med. Chem. 43 (2) (2008) 2831–2834.
- [9] D. Secci, A. Bolasco, P. Chimenti, S. Carradori, Curr. Med. Chem. 18 (2011) 5114–5144.
- [10] A. Musa, H.S. Abulkhair, A. Aljuhani, N. Rezki, M.A. Abdelgawad, K. Shalaby, A. H. El-Ghorab, M.R. Aouad, Pharmaceuticals 16 (2023) 463.
- [11] K. Karrouchi, I. Celik, S. Fettachc, T. Karthick, K. Bougrine, S. Radi, My El Abbes Faouzi, M. Ansar, R. Renjithi, J. Mol. Struct. 1265 (2022) 133363.
- [12] A.H. Abdelazeem, A.G. Safi El-Din, H.H. Arab, M.T. El-Saadi, S.M. El-Moghazy, N. H. Amin, J. Mol. Struct. 240 (2021) 130565.

- [13] N.M. Mallisetty, H. Ganipisetti, D. Majhi, R. Sirisilla, V.N. Kumar Putta, Curr. Drug Discov. Technol. 20 (2) (2023) 41–52.
- [14] D.M. Ahmed, J.M. Chen, A.D.A.R. Sanders, Pharmaceuticals 15 (2022) 197.
- [15] J.L. Liu, B. Yan, J. Phy. Chem. 112 (2008) 14168.
- [16] Audrieth, J. Org. Chem. 19 (1954) 288.
- [17] A.R. Sameh, A.E. Amira, M.M. Marwa, J. Heterocyclic Chem. 54 (6) (2017) 3358–3371.
- [18] M.S. Mohamed, Y.M. Zohny, W.M. El-Senousy, A.M. Abou, Pharmacophore 9 (1) (2018) 126–139.
- [19] A.M. Al-Qaaneh, T. Alshammari, R. Aldahhan, H. Aldossary, Z.A. Alkhalifah, J. F. Borgio, Saudi. J. Biol. Sci. 28 (3) (2021) 1978–1989.
- [20] Z. Yang, P. Li, X. Gan, Molecules 23 (7) (2018) 1798, https://doi.org/10.3390/molecules23071798.
- [21] O. Esteban, S. Katherine, G. Lenin, R. Mario, P.G. Linda, C.K. Nikolaos, M. Claire, G.J. Ana María, B. Carlos, C. Doménica, S. Hugo, U. Luis, Z. Rasa, G. Naomi, L. Andrés, Diagn. Microbiol. Infect. Dis. 98 (1) (2020) 0732–8893, https://doi.org/10.1016/j.diagmicrobio.2020.115094.
- [22] G. Mehreen, U. Mehran, A. Haider Khan, G. Sabreen, A.M.S. Muhammad, Q. Syed, S. Syed, B. Simona, Bioengineering 10 (2023) 100, https://doi.org/10.3390/ bioengineering10010100.
- [23] C. Liu, Q. Zhou, Y. Li, L.V. Garner, S.P. Watkins, L.J. Carter, J. Smoot, A.C. Gregg, A.D. Daniels, S. Jervey, ACS Cent. Sci. 6 (2020) 315–331.
- [24] A. Zumla, J.F. Chan, E.I. Azhar, D.S. Hui, K.Y. Yuen, Nat. Rev. Drug Discov. 15 (2016) 327–347.
- [25] A. Zhavoronkov, J. Chem. Inf. Model. 60 (2020) 2657-2659.
- [26] A.H. De Wilde, E.J. Snijder, M. Kikkert, M.J. van Hemert, Host factors in coronavirus replication. Roles of host gene and non-coding RNA expression in virus infection, 2018, 1–42.
- [27] K. Uzunova, E. Filipova, V. Pavlova, T. Vekov, Biomed. Pharmacother. 131 (2020) 110668.
- [28] Y.L. Weng, S.R. Naik, N. Dingelstad N, M.R. Lugo, S. Kalyaanamoorthy S, A. Ganesan, Sci. Rep. 11 (1) (2021) 7429.
- [29] J. Haribabu, V. Garisetti, R.E. Malekshah, S. Srividya, D. Gayathri, N. Bhuvanesh, R. Karvembu, J. Mol. Struct. 1250 (2022) 131782.
- [30] A. Musa, H.S. Abulkhair, A. Aljuhani, N. Rezki, M.A. Abdelgawad, K. Shalaby, M. R. Aouad, Pharmaceuticals 16 (3) (2023) 463.
- [31] M. Marinescu, Antibiotics 12 (7) (2023) 1220.
- [32] S. Abu-Melha, M.M. Edrees, S.M. Riyadh, M.R. Abdelaziz, A.A. Elfiky, S.M. Gomha, Molecules 25 (19) (2023) 4565.
- [33] S. Chatterjee, N. Kumar, H. Sehrawat, N. Yadav, V. Mishra, Curr. Res. Green Sustainable Chem. 4 (2021) 100064.
- [34] A. Barakat, A.M. Al-Majid, B.M. Al-Qahtany, M. Ali, M. Teleb, S.Naz Al-Agamy, Z. Ul-Haq, Chem. Cent. J. 12 (2005) 29.
- [35 Asma, B. Kalluraya, N. Manju, Der. Pharma. Chemica 9 (2017) 50.
- [36] S. Shetty, B. Kalluraya, S.K. Nithinchandra, S.B.Telkar Peethambar, Med. Chem. Res. 23 (2014) 2834.
- [37] K.S. Dhaka, Jag Mohan, V.K. Chanda, H.K. Pujari, Indian J. Chem. 12 (1974) 288.
- [38] Bruker. SAINT, 'Data Reduction Software', Bruker AXS Inc., Madison, WI, USA, 2009.
- [39] M.A. Spackman, D. Jayatilaka, Cryst. Eng. Comm. 11 (2009) 19–32.

- [40] J.J. McKinnon, D. Jayatilaka, M.A. Spackman, Chem. Commun. (2007) 3814–3816.
- [41] M.J. Frisch, G.W. Trucks, H.B. Schlegel, G.E. Scuseria, M.A. Robb, J.R. Cheeseman, G. Scalmani, V. Barone, G.A. Petersson, H. Nakatsuji, X. Li, M. Caricato, A. Marenich, J. Bloino, B.G. Janesko, R. Gomperts, B. Mennucci, H.P. Hratchian, J.V. Ortiz, A.F. Izmaylov, J.L. Sonnenberg, D. Williams-Young, F. Ding, F. Lipparini, F. Egidi, J. Goings, B. Peng, A. Petrone, T. Henderson, D. Ranasinghe, V.G. Zakrzewski, J. Gao, N. Rega, G. Zheng, W. Liang, M. Hada, M. Ehara, K. Toyota, R. Fukuda, J. Hasegawa, M. Ishida, T. Nakajima, Y. Honda, O. Kitao, H. Nakai, T. Vreven, K. Throssell, J.A. Montgomery, Jr., J.E. Peralta, F. Ogliaro, M. Bearpark, J. J. Heyd, E. Brothers, K.N. Kudin, V.N. Staroverov, T. Keith, R. Kobayashi, J. Normand, K. Raghavachari, A. Rendell, J.C. Burant, S.S. Iyengar, J. Tomasi, M. Cossi, J.M. Millam, M. Klene, C. Adamo, R. Cammi, J.W. Ochterski, R.L. Martin, K. Morokuma, O. Farkas, J.B. Foresman, D.J. Fox, Gaussian 09 Gaussian, Inc., 2016, Wallineford CT.
- [42] T. Lu, F. Chen, Multiwfn: a multifunctional wavefunction analyzer, J. Comput. Chem. 33 (2012) 580–592.
- [43] W. Humphrey, A. Dalke, K. Schulten, VMD: visual molecular dynamics, J. Mol. Graph. 14 (1996) 33–38.
- [44] G.M. Morris, R. Huey, W. Lindstrom, M.F. Sanner, R.K. Belew, D.S. Goodsell, A. J. Olson, Autodock4 and AutoDockTools4: automated docking with selective receptor flexibility, J. Comput. Chem. 16 (2009) 2785–2791.
- [45] P. Mee-udorn, K. Phiwkaow, R. Tinikul, K. Sanachai, S. Maenpuen, T. Rungrotmongkol, ACS Omega 8 (2023) 35580–35591.
- [46] U. Yadava, H. Gupta, M. Roychoudhury, Med. Chem. Res. 21 (2012) 2162-2168.
- [47] K.J. Bowers, E. Chow, Huafeng Xu, Ron O. Dror, M.P. Eastwood, B.A. Gregersen, J. L. Klepeis, I. Kolossvary, M.A. Moraes, F.D. Sacerdoti, J.K. Salmon, Y. Shan, D. E. Shaw, Scalable algorithms for molecular dynamics simulations on commodity clusters, in: Proceedings of the ACM/IEEE Conference on Supercomputing (SC06), Tampa, Florida, 2006. November 11-17.
- [48] G.M. Sheldrick, Acta. Cryst. A64 (2008) 112-122.
- [49] A.L. Spek, PLATON, Acta. Cryst. A46 (1990) c34.
- [50] C.F. Macrae, I.J. Bruno, J.A. Chisholm, P.R. Edgington, P. McCabe P, E. Pidcock, L. Rodriguez-Monge, R. Taylor, J. van de Streek, P.A. Wood, J. Appl. Cryst. 41 (2008) 466–470.
- [51] D.V. Geetha, A. Fares Hezam, H.E.M. Yasser, M.A. Sridhar, A.K. Shaukath, N. K. Lokanath, J. Mol. Struct. 178 (2019) 384–393, https://doi.org/10.1016/j.molstruc.2018.10.016.
- [52] Jun-ichi Aihara, Theor. Chem. Acc. 102 (1999), 134e138.
- [53] E.R. Johnson, S. Keinan, P. Mori-Sánchez, J. Contreras-García, A.J. Cohen, W. Yang, J. Am. Chem. Soc. 132 (2010) 6498–6506.
- [54] M. Kavimani, V. Balachandran, B. Narayana, K. Vanasundari, B. Revathi, Acta. A. Mol. Biomol. Spectrosc. 190 (2018) 47–60.
- [55] M. Toy, H. Tanak, Acta. A. Mol. Biomol. Spectrosc. 152 (2016) 530-536.
- [56] J.H. Beigel, K.M. Tomashek, L.E. Dodd, A.K. Mehta, B.S. Zingman, A.C. Kalil, H. C. Lane, N. Engl. J. Med. 383 (19) (2020) 1813–1826.
- [57] S. Bharadwaj, A. Dubey, U. Yadava, S.K. Mishra, S.G. Kang, V.D. Dwivedi, Brief. Bioinformatics 22 (2) (2021) 1361–1377.
- [58] A. Singh, S. Kumar, V.K. Gupta, S. Singh, V.D. Dwivedi, U. Mina, J. Biomol. Struct. Dyn. 41 (11) (2023) 4903–4916, https://doi.org/10.1080/ 07391102.2022.2074142.